Astron. Astrophys. 335, 637–646 (1998)

ASTRONOMY AND ASTROPHYSICS

# Limb-darkening and radii of non-Mira M giant models

**K.-H. Hofmann**[1] **and M. Scholz**[2]

[1] Max-Planck-Institut für Radioastronomie, Auf dem Hügel 69, D-53121 Bonn, Germany
[2] Institut für Theoretische Astrophysik der Universität Heidelberg, Tiergartenstr. 15, D-69121 Heidelberg, Germany

Received 22 January 1998 / Accepted 30 March 1998

**Abstract.** Monochromatic limb-darkening and monochromatic radii predicted by the non-Mira M giant models of Bessell et al. (1989a, 1991) with 3500 K $\geq$ T$_{eff}$ $\geq$ 2500 K were computed for selected typical bandpasses used in interferometric and lunar occultation work. Problems of defining and measuring radii of extended-photosphere stars and the relationship between different assumptions on limb-darkening and 'measured' radii are discussed.

Fits of simple uniform disk (UD), fully darkened disk (FDD) and Gaussian limb-darkening curves to the visibilities predicted by the non-Mira M giant models were performed. These fits show that the FDD curve is often a surprisingly good approximation to the model-predicted limb-darkening shape.

**Key words:** techniques: interferometric – stars: AGB – stars: atmospheres – stars: late-type

## 1. Introduction

Observing a star's diameter by interferometric or lunar occultation techniques means observing the interference or the diffraction pattern produced by the center-to-limb variation (clv) or limb-darkening of the intensity emitted by the star towards the observer. Since reconstruction of the clv from this pattern is extremely difficult and has only attempted for a very few of the brightest and largest stars the standard procedure of reducing interferometric or lunar occultation data means fitting a model-predicted pattern to the observed pattern within certain limits of accuracy. Though M type giants are among the most frequently observed stars model-predicted clv curves are only available for early to middle M spectral types with $T_{eff}$ $\geq$3500 K in the literature (Manduca et al. 1977, Manduca 1979, Van Hamme 1993, Diaz-Cordoves et al. 1995, Claret et al. 1995). According to standard calibrations (Ridgway et al. 1980, Di Benedetto 1993, Dyck et al. 1996) T$_{eff}$ = 3500 K corresponds to about M4 to M5III stars. Hence, observational data of middle to late M type giants have to be reduced by means of artificial clv curves, in particular the uniform disk (UD), fully darkened disk (FDD) or Gauss disk approximations introducing hardly predictable errors. Model limb-darkening shapes published by Scholz & Takeda (1987) are sometimes used by observers which, however, are just illustrative examples of selected models and filters and are poorly suited for systematic data reduction.

We shall give in this paper clv curves of typical filters for a model grid of non-Mira middle to late M type giants, and we shall discuss how model-predicted and artificial clv curves are correlated with 'measured' monochromatic radii. Equivalent data based on selected models of Mira variables will be provided in a forthcoming paper (K.-H. Hofmann, M. Scholz & P.R. Wood, in preparation, henceforth called HSW). For a general discussion of problems of limb-darkening and stellar radius determination we refer to the recent review of Scholz (1997). Reconstruction of empirical clv shapes was attempted by Bogdanov & Cherepashchuk (1990) from lunar occultation data of the SRb variables FY Lib (M5III) and SW Vir (M7III).

*Send offprint requests to*: K.-H. Hofmann

## 2. Models

This study uses the static M giant and supergiant model grid of BBSW (Bessell et al. 1989a, 1991) which includes three series of solar-composition stars with 1 M$_{\odot}$ and three different luminosities, $10^4$ L$_{\odot}$ (X series), $2 \times 10^3$ (Z series), $5 \times 10^2$ (U series), ranging from $T_{eff} = 3500\,K$ to $2500\,K$. As late M type giants have non-negligible photospheric extension each model of each series is described by three parameters $T_{eff}$, $log\,g$ and $D = T_{eff}/(g \cdot R)$ where $D$ is an extension-related quantity. These parameters are listed by BBSW who adopt the layer with unity Rosseland optical depth for defining the stellar radius: $R = r(\tau_{Ross} = 1)$. Its relation to observable stellar radii will be discussed in Sect. 4. BBSW also list a Rosseland extension $d = (r(\tau_{Ross} = 10^{-5}) - R)/R$ but one should be aware that Rosseland opacities in upper layers may significantly depend on the completeness and accuracy of molecular line data and on the technique of statistically treating line contributions, and that the Rosseland optical depth scale is just a computational scale without significant physical meaning in the upper photosphere. A more physical description of photospheric extension is given by the position of the layers of formation of the strongest molecular absorption bands as discussed in Sect. 5.

Physical assumptions and numerical construction of the model grid, including limitations and accuracies, are described

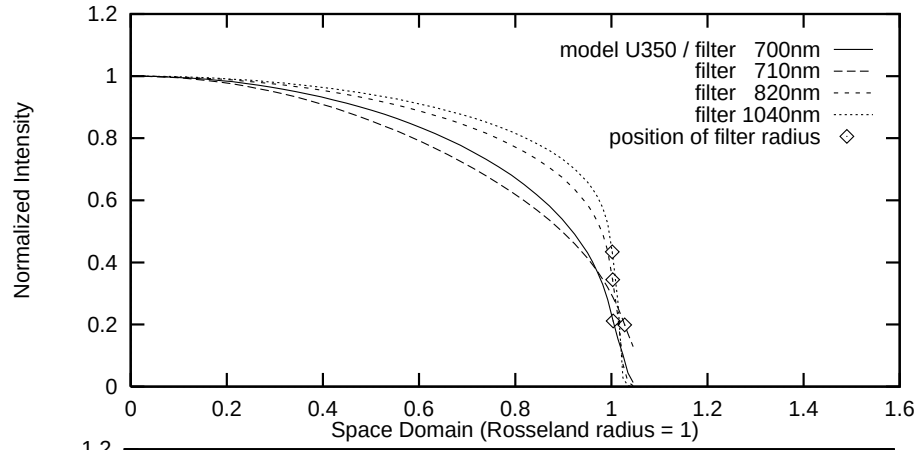


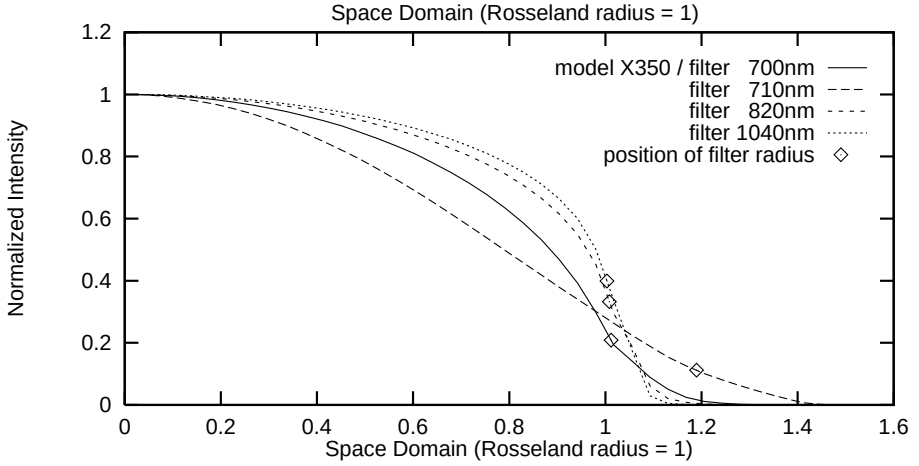


**Fig. 1.** Center-to-limb variation for the static models: U350 and X350 (Fig. 1 top and bottom) U300 and X300 (Fig. 2 top and bottom), and U250 and X250 (Fig. 3 top and bottom). The lower 400 nm curves in Fig. 2 are for strict LTE (see text). The abscissa are in units of the Rosseland radius $R = r(\tau_{Ross} = 1)$. The diamonds give the positions of the filter radii $R_{fil}$ after Scholz & Takeda (1987).

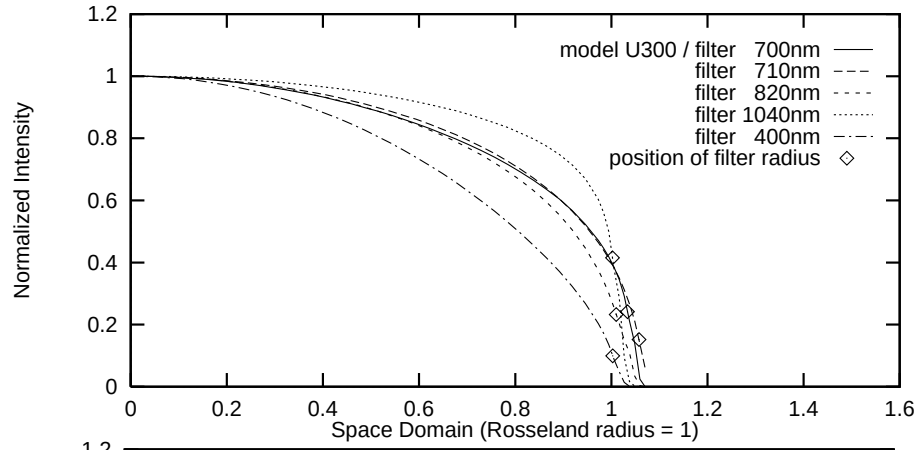


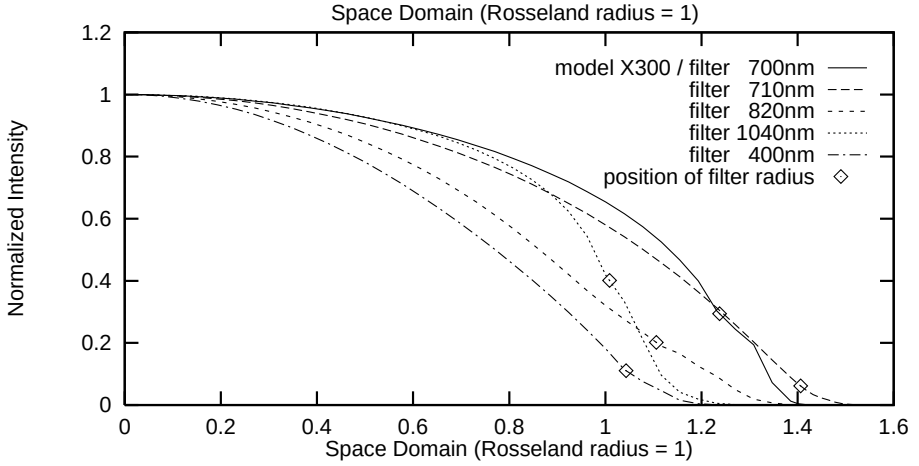


**Fig. 2.** See caption to Fig. 1.

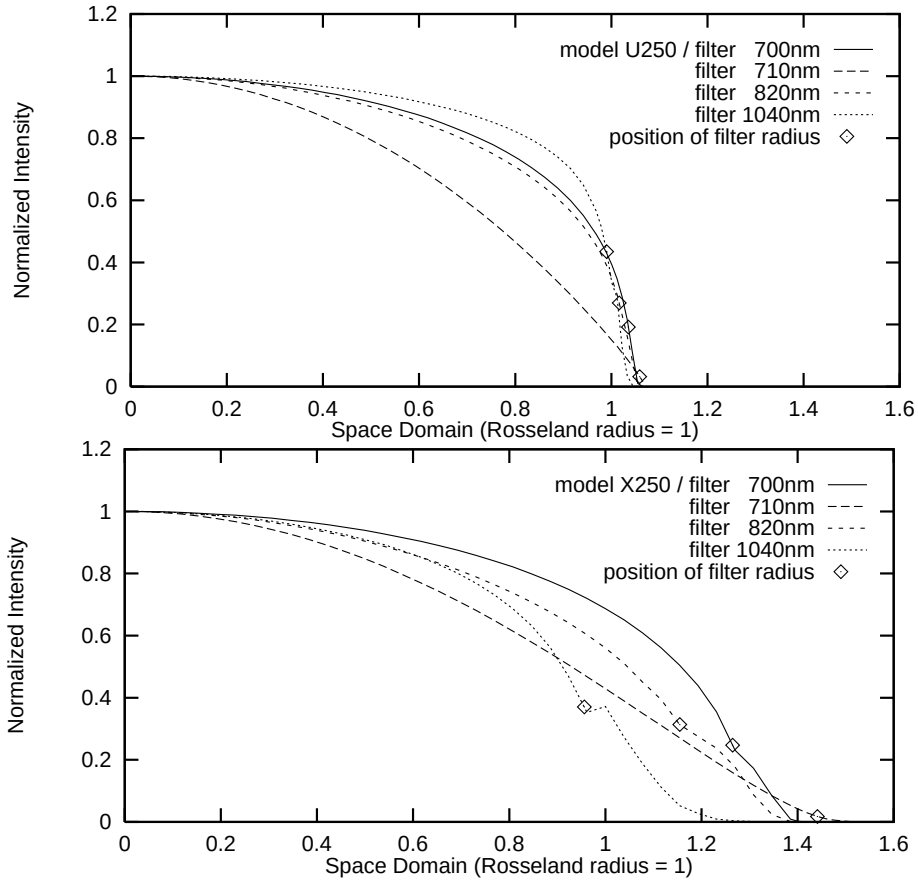


**Fig. 3.** See caption to Fig. 1.

in detail in BBSW. We wish to mention in particular that TiO bands are treated in the simple JOLA approximation which tends to overestimate strengths of saturated bands so that limb-darkening curves and monochromatic radii predicted for strong-TiO filters at low temperatures must be regarded with caution.

The parameters of the model series allow convenient interpolation of observable photospheric features like colors or clv shapes to actual evolutionary tracks as described by BBSW. Since clv shapes essentially depend on the parameters $T_{eff}$ and D simplified interpolation in only these two quantities is usually sufficient and might even be justified as a fair approximation for semi-regular variables whose photospheres are affected but probably not dominated by dynamical effects yielding larger $D_{eff} = T_{eff}/(g_{eff} \cdot R) > D$ due to lower effective gravity $g_{eff} < g$. The $D$ values of X models are 2.2 times those of Z models and 4.5 times those of U models at fixed $T_{eff}$, and low-temperature X models have Rosseland extensions of the order of 0.5 as well as significant extensions in terms of molecular band formation. Mira variables whose photospheres are dominated and strongly inflated by outward travelling shock fronts will be treated in the forthcoming HSW (in prep.) study.

## 3. Filters

Programs of interferometric radius measurements prefer filters at small wavelengths in order to secure sufficient angular resolution. Typically, filters are in the 0.4 to 1.0$\mu$m range. Unfortunately, broad real-continuum windows are only found at the two edges of this range in late M type giants where the 0.4$\mu$m region is in the Wien drop of the spectrum and emits very few photons and the 1.0$\mu$m region is outside the sensitivity range of optical detectors. Several near-continuum windows are also found at wavelengths in between, but these windows require fairly narrow filter bandpasses for useful near-continuum observation and become more and more affected by molecular band absorption with decreasing effective temperature and increasing geometric extension (see, e.g., the spectrum discussions of BBSW, Bessell et al. 1989b, 1996).

Lunar occultation radii are usually observed in infrared broad-band continuum filters, in particular in H and K, as well as in L$^*$ which is a slightly water- contaminated continuum filter with less contamination than the conventional L filter.

We are, of course, in no position to present limb-darkening data for those many dozens of filters used in past and future observational programs. Instead, we have chosen a set of representative narrow- and broad-band filters which demonstrate typical effects in different models, and we offer to provide upon request limb-darkening data for specific filters when these are needed for reduction of observational data of a star whose parameters are expected to lie within a specified range of our model grid. Our filters are listed in Table 1. The TiO-affected filters from 0.58 to 0.92$\mu$m are strictly monochromatic with formal 1 nm full widths. They cover near-continuum, moderate-TiO and strong-TiO features where the strength of TiO absorption depends on

**Table 1.** Filters. Bandpasses are rectangular. Central wavelengths $\lambda_c$ and full widths $\Delta\lambda$ are in $\mu$m.

| Name | Feature | $\lambda_c$ [$\mu$m] | $\Delta\lambda$ [$\mu$m] |
|---|---|---|---|
| 0.40 | continuum | 0.405 | 0.01 |
| 0.58 | near-continuum to moderate-TiO | 0.5805 | 0.001 |
| 0.59 | moderate-TiO to strong-TiO | 0.5895 | 0.001 |
| 0.70 | near-continuum to moderate-TiO | 0.7015 | 0.001 |
| 0.71 | moderate-TiO strong-TiO | 0.7100 | 0.001 |
| 0.75 | near-continuum to moderate-TiO | 0.7500 | 0.001 |
| 0.82 | near-continuum | 0.8185 | 0.001 |
| 0.92 | near-continuum | 0.9195 | 0.001 |
| 1.04 | continuum | 1.0465 | 0.001 |
| 1.63 H | continuum | 1.633 | 0.30 |
| 2.20 K | continuum | 2.195 | 0.40 |
| 3.80 L* | (impure) continuum | 3.799 | 0.60 |

effective temperature and geometric extension. For the broad 0.40 and 1.04$\mu$m continuum windows any reasonably chosen filter bandpasses yield identical clv shapes. The centers and widths of our three broad-band infrared filters are those listed by BBSW, and resulting limb-darkening curves hardly differ from curves obtained with more sophisticated (non-rectangular) H, K and L* filter transmissions.

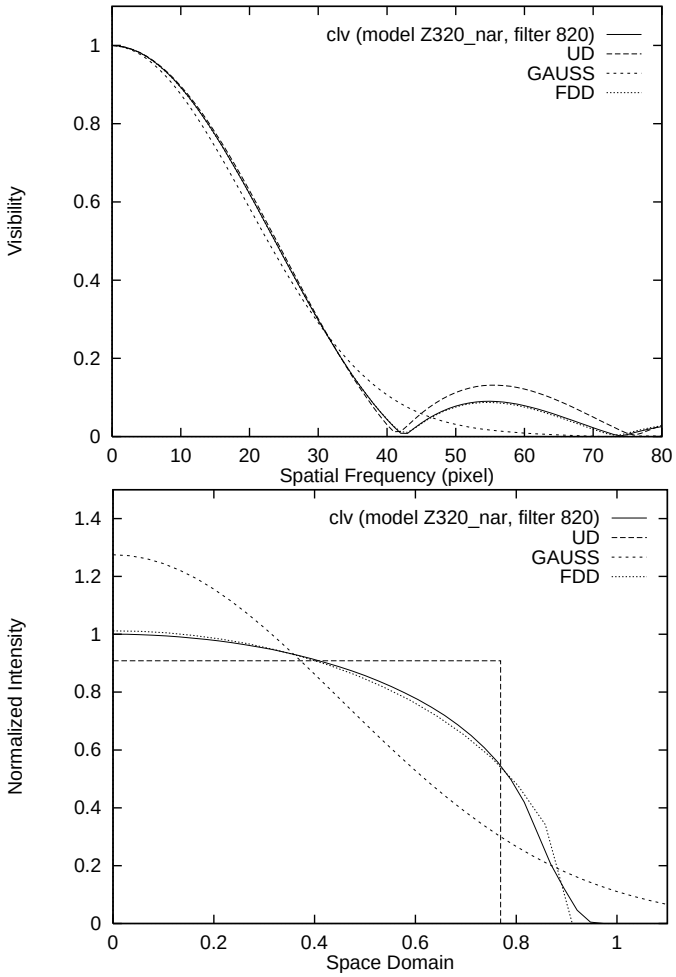


**Fig. 4.** Model Z320: (top) visibility plus the fitted visibilities of UD, FDD and Gaussian (visibility distances: 0.50%, 0.05% and 2.40%), (bottom) *true* clv plus clv of UD, FDD and Gaussian (with identical integrated intensities; clv distances: 15%, 2% and 19%). The artificial clv's UD, FDD and Gaussian displayed have not the same central intensity as the *true* clv, but they are all normalized to have the same integrated intensity value. Integral intensity normalization means the same visibility value at zeroth frequency for all these clv's. Integral intensity normalization is applied since integral visibility normalization (i.e. conventional central intensity normalization) requires the knowledge of the Fourier spectrum over the whole u-v plane, which observationally is not achievable.

## 4. Stellar monochromatic radii

In stars with compact photospheres clv curves drop steeply near the limb of the stellar disk and the stellar photospheric radius may safely be defined as the distance r from the disk's center where the intensity $I(r)$ reaches a near-zero level. In case of the Sun whose clv can be observed in detail the $I(r)$ inflection point resulting from tiny light contributions of outermost atmospheric layers defines the solar photospheric radius. Common parameterized clv approximations (see Scholz 1997) like the uniform or the fully darkened disk use the variable $\mu = (1-r^2/R^2)^{1/2}$ and reach zero intensity $I(\mu)$ at $\mu = 0$ (involving a discontinuity at the edge, see Sect. 6). Since extinction coefficients as well as source functions vary with wavelength, clv shapes depend on wavelength, and filter-independence of diameters measured in different bandpasses is a robust test of the quality of the adopted limb-darkening.

If the star's photosphere is a spherically extended configuration a specific layer has to be *chosen* whose distance $r$ from the star's center shall be called *the* stellar radius. Effective temperatures $T_{eff} \propto (L/R^2)^{1/4}$, 'surface' gravities $g \propto M/R^2$ and parameters $D = T_{eff}/(g \cdot R)$ then refer to this specific layer. Baschek et al. (1991) have summarized various radius definitions occurring in the literature. The above introduced Rosseland optical-depth radius, R = r($\tau_{Ross} = 1$), allows convenient comparison of observed stars with stellar interior models conventionally computed in the $\tau_{Ross}$ variable. This wavelenght-independent reference radius, however, is not directly related to observed center-to-limb intensity variations emitted by a star which are governed by the depth-dependence of the monochromatic $\tau_\lambda$ variable, i.e. of the monochromatic extinction coefficient at the wavelengths of observation. It is, therefore, customary in extended-photosphere work to introduce wavelength-dependent monochromatic optical-depth radii $R_\lambda$ = r($\tau_\lambda = 1$) besides the Rosseland reference radius R of the star referring to

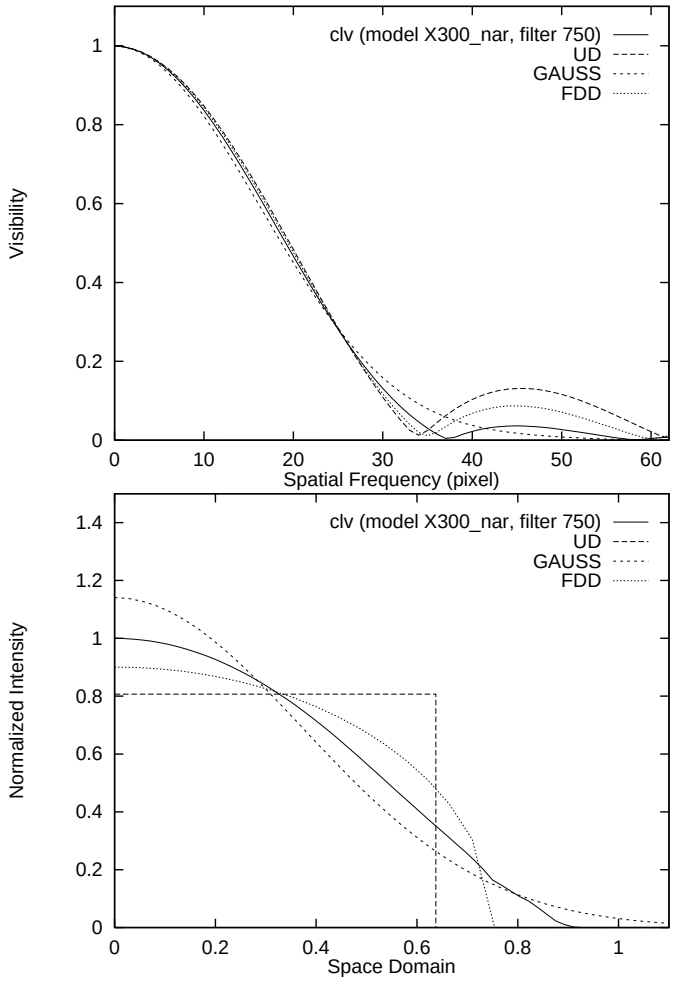


**Fig. 5.** Model X300: (top) visibility plus the fitted visibilities of UD, FDD and Gaussian (visibility distances: 1.10%, 0.70% and 1.30%), (bottom) *true* clv plus clv of UD, FDD and Gaussian (with identical integrated intensities; clv distances: 18%, 8% and 8%).

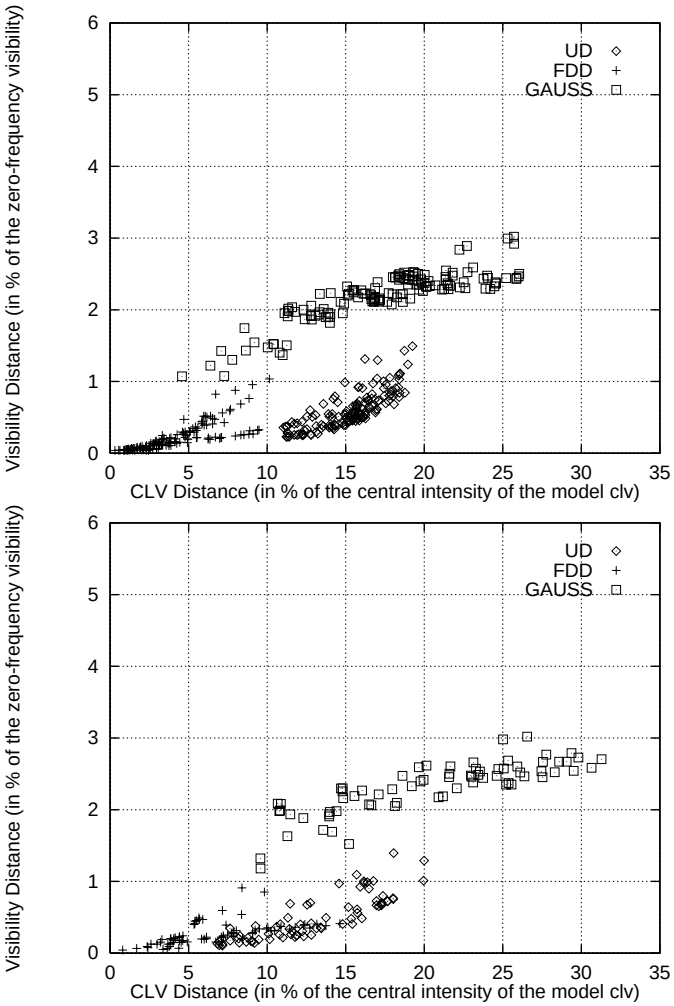


**Fig. 6.** Correlation between the visibility and clv distances derived from the visibility least-squares fit between the artificial models (UD, FDD, Gaussian) and all "true" limb-darkening curves (same fit range as in the Tables 2a to c, i.e. between frequency zero and the first local minimum of corresponding UD visibility). Top: all narrow-band filters. Bottom: all broad-band filters.

the $\tau_\lambda$ scale. (The fact that any actual observation is in bandpasses of final wavelength width within which the monochromatic extinction coefficient may vary appreciably sometimes leads to severe complications and to the below sketched problem of defining physically meaningful bandpass or filter radii $R_{fil}$.)

Though the monochromatic optical-depth radius $R_\lambda$ is more closely related to the clv than the reference radius R one must be aware that photons seen by the observer originate from a fairly wide range of depths around the $\tau_\lambda = 1$ layer (Scholz 1997) and that, due to the behavior of source functions and intensity contribution functions, there exists no trivial correlation between the shape of the limb-darkening curve and the position of the $\tau_\lambda = 1$ point on this curve. Fortunately, M giant continua are formed in fairly compact regions because of the steep temperature increase of the absorption coefficient towards deep layers (Scholz 1997) so that clv shapes are similar to those of compact photospheres and continuum radii are well-defined quantities. In contrast, clv shapes affected or dominated by molecular band absorption may have extended outer 'wings', and positions of $\tau_\lambda = 1$ points may be anywhere in the outer portions of the clv. The inflection point, for instance, has no special meaning in these cases, and even Gauss-type limb-darkening or slight limb-brightening may be found from models (e.g. Scholz & Takeda 1987, Scholz 1997, HSW in prep.) and observations (e.g. Tuthill et al. 1994, Haniff et al. 1995, HSW in prep.).

Observations that are aimed at determining effective temperatures have to involve a procedure which is called 'scaling' in the literature and which converts the observational data into *the* stellar radius. Conventionally, the $\tau_{Ross} = 1$ layer is chosen for this purpose as $\tau_{Ross}$ is a standard modelling scale and as this layer is close to $\tau_{cont} = 1$ layers in non-Mira M giants. This 'scaling' procedure does, in fact, account for two and often three different effects. First: conversion of a radius quantity derived by adopting an artificial (e.g. UD) limb-darkening law into the $\tau_{cont} = 1$ radius taken from a model with model-predicted

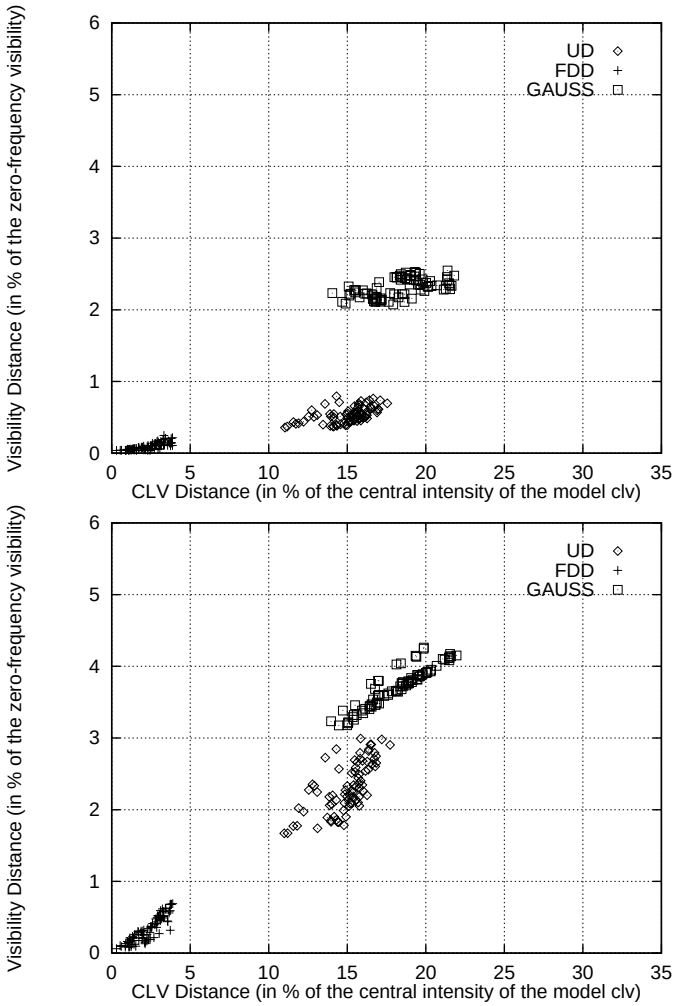


**Fig. 7.** Correlation as in Fig. 6 (top), but for those distances pairs only where the "true" limb-darkening curve is nearly a perfect FDD (i.e. FDD clv distances smaller than 4%). Top: fit range from frequency zero to the first local minimum of the corresponding UD visibility (including the central maximum only). Bottom: fit range twice as large, i.e. including central and first maxmimum of the corresponding UD visibility.

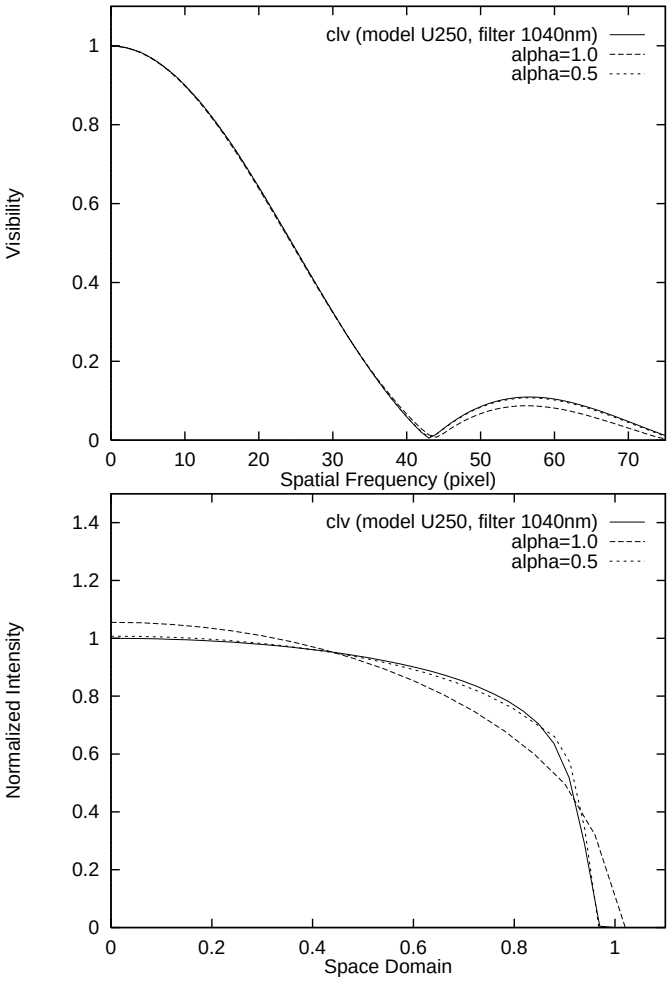


**Fig. 8.** Model U250: (top) visibility plus the fitted visibilities of the best-fitting power law model ($\alpha$=0.5) and the FDD (visibility distances: 0.04% and 0.25%), (bottom) *true* clv plus clv of the power law model with $\alpha$=0.5 and FDD (with identical integrated intensities; clv distances: 1.5% and 8.3%).

realistic limb-darkening. This conversion also applies to compact photospheres and should in this case result in wavelength-independent monochromatic radii. Second: conversion of the $\tau_{cont} = 1$ radius into the $\tau_{Ross} = 1$ radius of the model. This step usually involves only small and safe scaling factors, but problems may occur for very cool Miras below $T_{eff} = 2500\,K$ where molecular band contributions to deep-layer Rosseland opacities are non-negligible (HSW in prep.). Third: preceding conversion of a near-continuum $\tau_\lambda = 1$ radius affected by molecular band absorption into the $\tau_{cont} = 1$ radius at this wavelength (or directly into $\tau_{Ross} = 1$) in those frequent cases where observations in real-continuum filters are not available. This conversion is not small and not harmless in cases of significant band contribution and noticeable photospheric extension so we decided to include a few common near-continuum bandpasses in our filter set.

Bandpasses of our set are so chosen that these are 'pure' filters not assembling photons from both high-intensity and low-intensity spectral features originating from deep and high layers, respectively. Only the L$^*$ continuum filter is slightly water-contaminated. We strongly warn against using impure filters in monochromatic radius observations of spherically extended photospheres. First, of course, there exists no physical $\tau_{filter} = 1$ radius as the extinction coefficient varies with wavelength within the bandpass. Scholz & Takeda (1987) have suggested to use a central-intensity-weighted mean of monochromatic radii $R_\lambda$ for defining a filter radius $R_{fil}$. Though this definition is widely used in the literature this 'radius' has no real physical meaning but is just a convenient reference quantity, and any other sensible $R_{fil}$ definition (e.g. flux-weighted mean of $R_\lambda$, $\tau = 1$ layer for bandpass-averaged extinction, ...) may serve the same purpose. Second, clv curves generated by mixtures of deep- and high-layer photons strongly depend on the details of the spectrum and of the filter transmission function and may have unusual shapes near the stellar limb. While

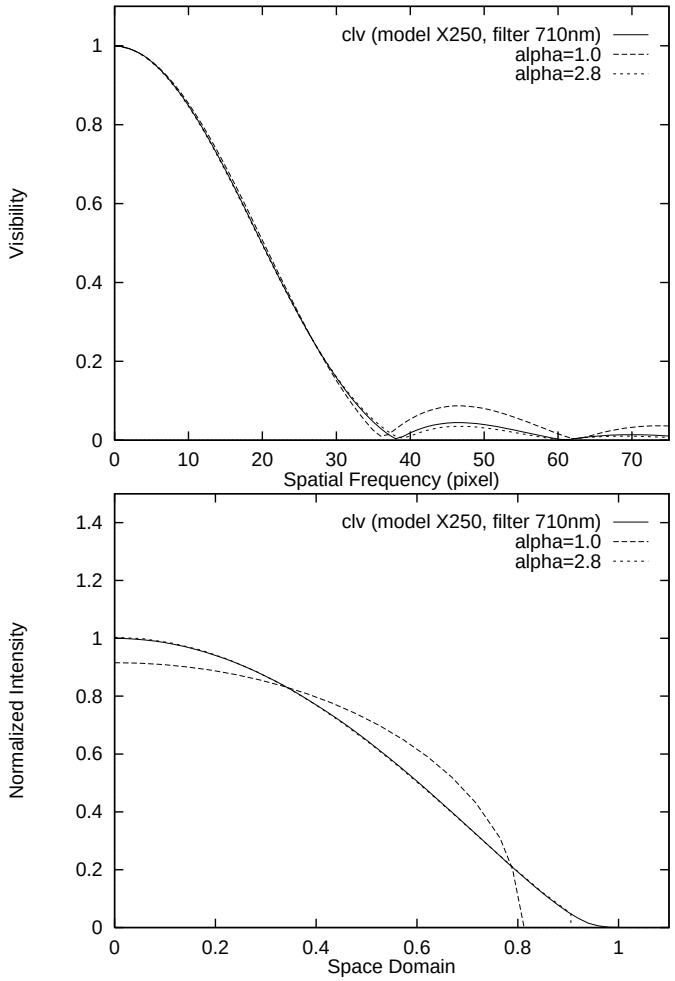


**Fig. 9.** Model X250: (top) visibility plus the fitted visibilities of the best-fitting power law model ($\alpha$=2.8) and the FDD (visibility distances: 0.05% and 0.61%), (bottom) *true* clv plus clv of the power law model with $\alpha$=2.8 and FDD (with identical integrated intensities; clv distances: 0.2% and 7.7%).

near-continuum filters containing moderate contaminations by neighboring bands do not pose significant problems, filters designed to probe the layers of molecular band formation should be as pure as possible. Noticeable 'leaking' of filter transmission at adjacent continuum wavelengths may result in hardly interpretable 'radius' measurements in case of large band versus continuum intensity contrast. Observers who want us to compute limb-darkening (as offered in Sect. 3) for an impure TiO band filter should provide a very accurate transmission curve extending well below the 1% level in the wings.

In principle, no molecular band filter is pure in a strict sense as it assembles light from both the lines and the gaps between lines. The more spaced the lines are the more the clv curve is dominated by continuum photons and the measured 'radius' approaches the continuum radius although the bandpass is evidently placed within the absorption band in the spectrum. Thus, spacing of molecular lines should be checked spectroscopically in case of doubt. TiO lines lie sufficiently close for measuring meaningful TiO band radii but, for instance, CO bands are little suited for radius observation.

## 5. Monochromatic limb-darkening and monochromatic radii

Monochromatic radii, i.e. filter radii $R_{fil}$ after Scholz & Takeda (1987), in units of stellar radii $R$ are listed in Table 2 for all models and all filters. Stellar radii are defined by the distance of the $\tau_{Ross} = 1$ layer from the star's center, and model designations are those of BBSW (e.g. X350 means the $T_{eff} = 3500\,K$ model of the X series). Limb-darkening curves were computed for every model-filter-combination and are available in electronic form upon request.

Sample clv shapes are shown in Figs. 1 to 3 . Most of the curves differ slightly from those of classical compact photospheres and exhibit, for about constant (continuous) absorption, with increasing wavelength the typical trend towards the uniform disk essentially caused by the behavior of the Planck ratio $B_\lambda(T(\tau_\lambda = \mu))/B_\lambda(\tau_\lambda = 1)$ seen by the observer. At 0.40$\mu$m the limb-darkening curve is noticeably affected by Rayleigh scattering and would still be flatter in the strict LTE approximation where the source function is set equal to the Planck function (see example in Fig. 2). Deviations from the 'smooth' clv shape typical of compact configurations occur above r($\tau_\lambda = 1$) positions when semi-infinity does no longer hold in radiation transfer of rays emitted towards the observer and stratification details show up prominently. 'Spikes' seen in a few curves, e.g. in Fig. 3, are artifacts resulting from the relatively small numbers of model depth points chosen in these survey computations and become smooth 'wiggles' for finer stratification spacing. Since the numbers in Table 2 are hardly affected we kept them unchanged in the present grid. The formation of extended wings and more Gauss-like clv shapes is restricted to TiO bandpasses in the coolest and most extended models of this static grid in contrast to Miras where they are found quite commonly (Scholz & Takeda 1987, HSW in prep.). The R10 radius also entered in Table 2 marks the position of the 10% intensity level and is to give a rough idea of the position of the $R_{fil}$ point in the outer portions of the limb-darkening curve. A detailed discussion of the effects of extinction coefficients and source functions on the center-to-limb intensity variation was given by Scholz & Takeda (1987).

Since most past and current observational data have been and are being reduced by means of artificial standard approximations of limb-darkening we also provide in Table 2 UD, FDD and Gauss 'radii' for convenient reduction of such artificial to physically meaningful radii. Though for the non-Mira giants the Gauss approximation turns out to be inadequate in most cases we have kept it in the tables for convenient direct comparison with equivalent Mira tables (HSW in prep.). The Gauss 'radius' refers to the full half-width of Gauss profile, i.e. it is necessarily much smaller than any other radius and should only be used differentially with respect to other filters and models.

**Table 2..** Monochromatic radii in selected filters. First line: filter designations after Table 1. Following upper lines: model designation after BBSW and $R_{fil}/R$ ($R_{10}/R$) ratios (see text). Following lower lines: UD, FDD and Gauss radii in units of $R_{fil}$ obtained by fitting the central maximum of the model clv visibility by means of a UD, FDD and Gauss clv, plus accuracy value (average deviation between the *true* limb-darkening and the fitted artificial clv in the space domain in % of the central intensity of the *true* limb-darkening; see text).

| Filter | 0.40 | 0.58 | 0.59 | 0.70 | 0.71 | 0.75 | 0.82 | 0.92 | 1.04 | 1.63 H | 2.20 K | 3.80 L* |
|---|---|---|---|---|---|---|---|---|---|---|---|---|
| Model | | | | | | | | | | | | |
| X350 | 1.02 (1.08) | 1.02 (1.02) | 1.06 (1.03) | 1.01 (1.06) | 1.19 (1.18) | 1.01 (1.07) | 1.01 (1.05) | 1.01 (1.08) | 1.00 (1.02) | 0.98 (1.02) | 0.98 (1.00) | 0.99 (1.02) |
| | 0.89/16 | 0.84/15 | 0.78/16 | 0.89/14 | 0.80/19 | 0.91/13 | 0.93/12 | 0.94/11 | 0.94/11 | 0.95/11 | 0.96/8 | 0.97/7 |
| | 0.99/5 | 0.94/5 | 0.87/7 | 0.99/3 | 0.89/9 | 1.01/2 | 1.03/3 | 1.05/4 | 1.04/4 | 1.06/4 | 1.07/8 | 1.08/9 |
| | 0.62/11 | 0.58/11 | 0.54/9 | 0.62/14 | 0.55/6 | 0.63/17 | 0.64/18 | 0.65/20 | 0.65/20 | 0.65/20 | 0.66/23 | 0.67/25 |
| Z350 | 1.00 (1.02) | 1.01 (1.00) | 1.02 (1.01) | 1.01 (1.02) | 1.06 (1.08) | 1.00 (1.01) | 1.00 (0.99) | 1.01 (0.99) | 1.00 (0.99) | 0.99 (1.02) | 0.99 (0.91) | 1.00 (1.01) |
| | 0.86/18 | 0.85/17 | 0.82/18 | 0.89/15 | 0.84/18 | 0.91/14 | 0.92/14 | 0.93/12 | 0.93/12 | 0.93/12 | 0.95/9 | 0.96/7 |
| | 0.96/5 | 0.94/3 | 0.91/5 | 0.99/2 | 0.94/5 | 1.01/3 | 1.02/5 | 1.04/7 | 1.04/7 | 1.04/8 | 1.05/11 | 1.07/13 |
| | 0.59/14 | 0.59/15 | 0.56/13 | 0.61/18 | 0.58/13 | 0.62/21 | 0.64/22 | 0.64/25 | 0.64/25 | 0.65/25 | 0.65/28 | 0.66/30 |
| U350 | 1.00 (0.97) | 1.00 (0.99) | 1.01 (0.99) | 1.00 (0.95) | 1.03 (0.99) | 1.00 (0.92) | 1.00 (0.90) | 1.00 (0.87) | 1.00 (0.86) | 1.00 (0.92) | 1.00 (0.88) | 1.00 (0.82) |
| | 0.85/18 | 0.85/17 | 0.82/18 | 0.88/15 | 0.86/17 | 0.91/14 | 0.92/13 | 0.93/13 | 0.93/13 | 0.93/12 | 0.94/9 | 0.95/7 |
| | 0.95/4 | 0.94/3 | 0.92/5 | 0.99/1 | 0.96/2 | 1.01/5 | 1.02/7 | 1.03/9 | 1.03/9 | 1.04/10 | 1.05/13 | 1.06/15 |
| | 0.59/15 | 0.59/16 | 0.57/14 | 0.61/20 | 0.60/17 | 0.62/23 | 0.63/24 | 0.64/25 | 0.64/26 | 0.65/27 | 0.65/30 | 0.66/31 |
| X335 | 1.03 (1.10) | 1.11 (1.03) | 1.23 (1.14) | 1.04 (1.09) | 1.33 (1.34) | 1.01 (1.08) | 1.01 (1.10) | 1.01 (1.07) | 1.01 (1.01) | 0.98 (1.02) | 0.98 (1.00) | 0.99 (1.02) |
| | 0.90/17 | 0.75/17 | 0.74/19 | 0.86/16 | 0.82/18 | 0.90/14 | 0.93/13 | 0.94/12 | 0.94/11 | 0.94/11 | 0.96/8 | 0.97/7 |
| | 1.00/6 | 0.84/8 | 0.82/10 | 0.95/6 | 0.91/6 | 1.00/3 | 1.03/3 | 1.05/4 | 1.05/4 | 1.05/4 | 1.07/7 | 1.09/9 |
| | 0.63/11 | 0.52/7 | 0.51/5 | 0.59/11 | 0.57/12 | 0.62/15 | 0.64/17 | 0.65/19 | 0.65/20 | 0.65/20 | 0.66/23 | 0.67/25 |
| Z335 | 1.01 (1.05) | 1.04 (0.99) | 1.07 (1.05) | 1.02 (1.04) | 1.11 (1.07) | 1.01 (1.03) | 1.01 (1.02) | 1.01 (1.01) | 1.00 (1.01) | 0.99 (1.03) | 0.99 (0.95) | 1.00 (1.02) |
| | 0.87/17 | 0.80/18 | 0.80/19 | 0.86/16 | 0.86/17 | 0.90/14 | 0.91/13 | 0.93/12 | 0.93/12 | 0.93/11 | 0.95/9 | 0.96/7 |
| | 0.96/4 | 0.89/6 | 0.89/7 | 0.96/3 | 0.95/2 | 1.00/2 | 1.02/4 | 1.04/6 | 1.04/7 | 1.04/7 | 1.06/10 | 1.07/12 |
| | 0.60/14 | 0.55/11 | 0.55/10 | 0.59/15 | 0.59/17 | 0.62/19 | 0.63/21 | 0.64/24 | 0.64/24 | 0.64/25 | 0.65/28 | 0.66/29 |
| U335 | 1.00 (1.00) | 1.02 (0.97) | 1.03 (0.99) | 1.01 (1.00) | 1.05 (1.00) | 1.00 (0.99) | 1.00 (0.98) | 1.00 (0.97) | 1.00 (0.96) | 1.00 (0.99) | 1.00 (0.99) | 1.00 (0.96) |
| | 0.85/18 | 0.81/18 | 0.83/18 | 0.86/17 | 0.87/16 | 0.89/14 | 0.91/14 | 0.92/12 | 0.93/12 | 0.93/11 | 0.94/9 | 0.96/7 |
| | 0.95/4 | 0.91/6 | 0.92/5 | 0.96/2 | 0.97/1 | 1.00/3 | 1.01/5 | 1.03/8 | 1.04/9 | 1.04/9 | 1.05/12 | 1.07/14 |
| | 0.59/15 | 0.56/13 | 0.58/13 | 0.59/17 | 0.60/19 | 0.62/21 | 0.63/23 | 0.64/25 | 0.65/26 | 0.64/26 | 0.65/29 | 0.66/31 |
| X320 | 1.03 (1.14) | 1.24 (1.24) | 1.30 (1.33) | 1.19 (1.21) | 1.36 (1.33) | 1.05 (1.06) | 1.02 (1.11) | 1.02 (1.13) | 1.01 (1.08) | 0.98 (1.07) | 0.98 (1.02) | 0.99 (1.05) |
| | 0.90/16 | 0.82/18 | 0.86/16 | 0.82/19 | 0.86/16 | 0.85/16 | 0.91/14 | 0.94/13 | 0.95/12 | 0.94/11 | 0.96/9 | 0.98/8 |
| | 1.00/6 | 0.92/8 | 0.95/3 | 0.91/9 | 0.96/2 | 0.95/6 | 1.01/5 | 1.05/4 | 1.05/3 | 1.05/4 | 1.07/7 | 1.09/8 |
| | 0.62/11 | 0.57/9 | 0.59/15 | 0.57/7 | 0.59/17 | 0.58/11 | 0.62/14 | 0.65/17 | 0.65/19 | 0.65/19 | 0.66/22 | 0.68/23 |
| Z320 | 1.01 (1.01) | 1.08 (1.04) | 1.10 (1.11) | 1.06 (1.04) | 1.12 (1.14) | 1.02 (1.02) | 1.01 (1.05) | 1.01 (1.04) | 1.01 (1.04) | 0.99 (1.00) | 0.99 (1.00) | 1.00 (1.04) |
| | 0.87/17 | 0.83/18 | 0.86/16 | 0.84/18 | 0.89/15 | 0.87/15 | 0.90/15 | 0.92/13 | 0.94/11 | 0.93/12 | 0.95/9 | 0.96/8 |
| | 0.97/4 | 0.92/6 | 0.96/1 | 0.94/5 | 0.99/2 | 0.97/3 | 1.00/2 | 1.03/4 | 1.04/7 | 1.04/6 | 1.05/9 | 1.07/11 |
| | 0.60/14 | 0.57/12 | 0.59/18 | 0.58/13 | 0.61/20 | 0.60/16 | 0.62/19 | 0.64/22 | 0.64/24 | 0.64/24 | 0.65/26 | 0.66/28 |
| U320 | 1.00 (1.01) | 1.03 (1.00) | 1.04 (1.04) | 1.02 (0.99) | 1.05 (0.99) | 1.01 (1.01) | 1.00 (1.00) | 1.00 (0.99) | 1.00 (0.98) | 1.00 (1.00) | 1.00 (1.00) | 1.00 (0.99) |
| | 0.86/18 | 0.84/18 | 0.86/16 | 0.85/18 | 0.89/15 | 0.87/16 | 0.90/14 | 0.92/13 | 0.93/11 | 0.93/12 | 0.94/9 | 0.96/8 |
| | 0.96/4 | 0.93/5 | 0.96/0 | 0.95/3 | 0.99/4 | 0.97/1 | 1.00/3 | 1.02/6 | 1.04/9 | 1.03/8 | 1.05/10 | 1.07/12 |
| | 0.59/15 | 0.58/14 | 0.60/18 | 0.59/16 | 0.61/22 | 0.60/19 | 0.62/22 | 0.63/24 | 0.64/26 | 0.64/26 | 0.65/27 | 0.66/29 |
| X300 | 1.04 (1.15) | 1.28 (1.27) | 1.35 (1.30) | 1.24 (1.27) | 1.41 (1.34) | 1.17 (1.23) | 1.11 (1.18) | 1.05 (1.15) | 1.01 (1.07) | 0.98 (1.06) | 0.98 (1.09) | 0.99 (1.16) |
| | 0.91/16 | 0.88/16 | 0.84/16 | 0.91/15 | 0.80/17 | 0.84/18 | 0.87/17 | 0.92/16 | 0.95/12 | 0.95/13 | 0.97/11 | 1.01/13 |
| | 1.02/6 | 0.98/2 | 0.93/3 | 1.02/2 | 0.90/5 | 0.93/8 | 0.97/7 | 1.03/6 | 1.06/3 | 1.06/4 | 1.08/6 | 1.13/7 |
| | 0.63/11 | 0.61/17 | 0.58/16 | 0.63/17 | 0.55/14 | 0.57/8 | 0.60/10 | 0.64/13 | 0.66/18 | 0.66/16 | 0.67/18 | 0.70/19 |
| Z300 | 1.01 (1.01) | 1.09 (1.11) | 1.11 (1.11) | 1.08 (1.11) | 1.13 (1.08) | 1.05 (1.06) | 1.03 (1.05) | 1.01 (1.03) | 1.00 (1.05) | 0.99 (1.01) | 0.99 (1.04) | 0.99 (1.07) |
| | 0.88/17 | 0.88/16 | 0.87/15 | 0.89/15 | 0.86/16 | 0.85/17 | 0.88/16 | 0.91/14 | 0.94/11 | 0.93/12 | 0.94/11 | 0.97/10 |
| | 0.98/4 | 0.98/1 | 0.97/1 | 1.00/1 | 0.96/1 | 0.94/5 | 0.98/3 | 1.01/2 | 1.04/6 | 1.03/5 | 1.05/6 | 1.08/8 |
| | 0.61/14 | 0.61/19 | 0.60/19 | 0.62/19 | 0.60/19 | 0.58/14 | 0.61/17 | 0.63/19 | 0.64/24 | 0.64/22 | 0.65/23 | 0.67/25 |
| U300 | 1.00 (1.01) | 1.04 (1.05) | 1.05 (1.04) | 1.03 (1.04) | 1.06 (1.02) | 1.02 (1.01) | 1.01 (1.00) | 1.01 (1.00) | 1.00 (0.99) | 0.99 (1.01) | 1.00 (0.99) | 1.00 (1.05) |
| | 0.87/17 | 0.88/15 | 0.87/15 | 0.89/16 | 0.87/16 | 0.86/17 | 0.88/15 | 0.91/13 | 0.93/11 | 0.92/12 | 0.93/12 | 0.95/10 |
| | 0.97/3 | 0.98/1 | 0.97/1 | 0.99/2 | 0.97/2 | 0.96/2 | 0.99/1 | 1.01/4 | 1.04/9 | 1.02/6 | 1.04/7 | 1.06/10 |
| | 0.60/16 | 0.60/20 | 0.60/20 | 0.61/20 | 0.60/20 | 0.59/17 | 0.61/20 | 0.62/23 | 0.64/26 | 0.63/24 | 0.64/25 | 0.66/28 |
| X280 | 1.04 (1.16) | 1.31 (1.31) | 1.39 (1.30) | 1.26 (1.28) | 1.44 (1.36) | 1.22 (1.32) | 1.15 (1.27) | 1.10 (1.19) | 1.00 (1.10) | 0.97 (1.10) | 0.97 (1.19) | 0.97 (1.31) |
| | 0.93/16 | 0.87/16 | 0.79/16 | 0.91/14 | 0.77/18 | 0.88/17 | 0.90/17 | 0.92/17 | 0.96/13 | 0.96/15 | 0.99/16 | 1.07/17 |
| | 1.04/5 | 0.97/2 | 0.88/4 | 1.02/2 | 0.85/7 | 0.98/5 | 1.01/6 | 1.02/6 | 1.07/3 | 1.07/6 | 1.10/7 | 1.19/7 |
| | 0.64/11 | 0.60/17 | 0.55/14 | 0.63/18 | 0.53/11 | 0.61/12 | 0.63/11 | 0.64/11 | 0.66/17 | 0.66/14 | 0.69/14 | 0.73/15 |
| Z280 | 1.01 (1.00) | 1.10 (1.12) | 1.13 (1.06) | 1.09 (1.11) | 1.14 (1.12) | 1.07 (1.08) | 1.04 (1.09) | 1.02 (1.02) | 1.00 (1.06) | 0.99 (1.05) | 0.99 (1.09) | 0.99 (1.06) |
| | 0.89/17 | 0.88/15 | 0.84/16 | 0.90/15 | 0.82/17 | 0.87/16 | 0.89/16 | 0.90/15 | 0.94/12 | 0.92/14 | 0.94/13 | 0.98/13 |
| | 0.99/3 | 0.98/1 | 0.94/2 | 1.01/3 | 0.91/4 | 0.97/3 | 0.99/3 | 1.01/2 | 1.04/6 | 1.03/3 | 1.05/4 | 1.09/5 |
| | 0.62/15 | 0.61/20 | 0.58/18 | 0.62/21 | 0.57/15 | 0.60/16 | 0.61/17 | 0.63/18 | 0.65/23 | 0.64/20 | 0.65/21 | 0.67/23 |
| U280 | 1.00 (1.01) | 1.04 (1.05) | 1.05 (0.98) | 1.03 (1.04) | 1.06 (1.05) | 1.02 (0.99) | 1.01 (0.99) | 1.00 (0.99) | 1.00 (0.99) | 0.99 (0.99) | 0.99 (1.05) | 0.99 (1.03) |
| | 0.87/17 | 0.88/15 | 0.85/16 | 0.90/14 | 0.83/17 | 0.87/16 | 0.89/16 | 0.90/14 | 0.93/11 | 0.91/13 | 0.92/13 | 0.95/12 |
| | 0.97/3 | 0.98/2 | 0.94/1 | 1.00/4 | 0.93/3 | 0.97/1 | 0.99/1 | 1.01/3 | 1.04/9 | 1.01/4 | 1.03/5 | 1.06/8 |
| | 0.60/16 | 0.60/20 | 0.58/19 | 0.62/22 | 0.58/17 | 0.60/18 | 0.61/19 | 0.62/22 | 0.64/26 | 0.63/22 | 0.64/23 | 0.66/26 |
| X250 | 1.01 (1.13) | 1.32 (1.26) | 1.40 (1.21) | 1.26 (1.26) | 1.44 (1.32) | 1.24 (1.32) | 1.15 (1.30) | 1.10 (1.22) | 0.96 (1.11) | 0.95 (1.17) | 0.96 (1.27) | 0.96 (1.31) |
| | 0.96/16 | 0.84/16 | 0.73/17 | 0.90/14 | 0.73/18 | 0.88/16 | 0.93/16 | 0.94/16 | 0.98/14 | 0.98/18 | 1.03/20 | 1.13/20 |
| | 1.07/5 | 0.93/3 | 0.81/7 | 1.00/2 | 0.82/8 | 0.98/4 | 1.04/4 | 1.05/5 | 1.09/4 | 1.09/8 | 1.14/10 | 1.26/8 |
| | 0.66/12 | 0.58/15 | 0.50/10 | 0.62/18 | 0.51/9 | 0.61/15 | 0.64/15 | 0.65/13 | 0.68/16 | 0.68/10 | 0.71/10 | 0.78/11 |
| Z250 | 0.99 (1.05) | 1.11 (1.06) | 1.13 (1.07) | 1.09 (1.11) | 1.14 (1.05) | 1.07 (1.07) | 1.05 (1.05) | 1.03 (1.08) | 0.98 (1.05) | 0.98 (1.09) | 0.98 (1.05) | 0.99 (1.10) |
| | 0.91/16 | 0.85/16 | 0.77/17 | 0.90/14 | 0.77/18 | 0.87/16 | 0.90/15 | 0.91/16 | 0.94/13 | 0.92/15 | 0.94/16 | 0.99/15 |
| | 1.01/2 | 0.95/1 | 0.86/5 | 1.00/3 | 0.86/7 | 0.97/1 | 1.01/1 | 1.02/1 | 1.05/5 | 1.03/4 | 1.05/4 | 1.10/2 |
| | 0.63/17 | 0.59/18 | 0.54/13 | 0.62/21 | 0.54/11 | 0.60/18 | 0.63/19 | 0.63/19 | 0.65/23 | 0.64/17 | 0.65/18 | 0.68/21 |
| U250 | 0.99 (0.98) | 1.04 (0.99) | 1.05 (0.99) | 1.04 (1.04) | 1.06 (1.02) | 1.03 (0.98) | 1.02 (0.97) | 1.01 (0.98) | 0.99 (0.98) | 0.99 (0.97) | 1.00 (1.03) | 1.00 (0.99) |
| | 0.89/16 | 0.85/16 | 0.78/18 | 0.89/15 | 0.78/18 | 0.87/16 | 0.90/15 | 0.90/14 | 0.94/11 | 0.90/15 | 0.92/15 | 0.95/13 |
| | 1.00/1 | 0.94/1 | 0.87/5 | 0.99/4 | 0.87/6 | 0.97/1 | 1.00/3 | 1.01/3 | 1.04/8 | 1.01/2 | 1.03/3 | 1.06/7 |
| | 0.62/18 | 0.59/18 | 0.54/14 | 0.61/22 | 0.54/12 | 0.60/19 | 0.62/21 | 0.62/21 | 0.64/26 | 0.63/20 | 0.64/22 | 0.66/25 |

## 6. Visibility fits

We have restricted the present investigations to interferometric observations only since lunar occultation is (up to now) not used for really monochromatic observations and the conventional IR band observations are represented by nearly uniform disks.

In the scope of this paper we call the theoretical limb-darkening curves the *true* center-to-limb variation (=clv) of the observed star. From each *true* clv (for every model/filter combination) the visibility of the 2-dimensional intensity distribution was calculated: our observed data in this paper. The visibilities of the artificial limb-darkening curves UD, FDD and Gaussian were also calculated. With a least-squares fit the spatial frequency scaling factor of the artificial clv visibility applied to the *true* clv visibility was determined and hence in object space the artificial clv (UD, FDD, Gaussian) radius of the *true* limb-darkening curve. The only fit variable was the spatial frequency scaling factor. The height of the visbility was kept constant with the same value at zeroth frequency for the *true* and artificial clv

visibility. Since the visibility value at zeroth frequency is identical to the integrated disk intensity in object space, the same visibility value at zeroth frequency means that *true* and artificial clv have the same integrated disk intensity. Therefore, different limb-darkening curves have different central intensities, but the same integrated disk intensity. Integrated disk intensity normalization is applied since integrated visibility normalization, i.e. the conventional central disk intensity normalization, requires the knowledge of the visibility over the entire u-v plane which of course is not available. The accuracy of the visibility fit was monitored by the visibility distance, i.e. the average distance between the *true* and fitted artificial clv visibility in % of the visibility at zeroth spatial frequency. The fit range was between spatial frequency zero and about two times the frequency at half maximum of the *true* clv visibility (i.e. near the first local minimum of the corresponding UD visibility). We have chosen this fit range since most visibility data are recorded in this frequency region.

As accuracy value the average distance between the *true* limb-darkening curve and the artificial clv (UD, FDD, Gaussian) in object space was chosen: the coordinate axis of the artificial clv was scaled according to the spatial frequency scaling factor derived by the least-squares visibility fit, and the integrated intensity of the *true* and artificial clv was kept identical as discussed above. This accuracy value, called clv distance, is given in Table 2 in % of the central intensity of the *true* limb-darkening curve. Models with accuracy values between 0 to 4% are good, between 4 to 12% are fair, and with values larger than 12% are poor. The observer probably cannot derive these object space accuracy values from measured visibility data. As discussed below, to derive the above object space accuracy values from visibility data covering only the small spatial frequency region up to the first local minimum of the corresponding UD visibility, requires visibility errors less $\sim 0.3\%$ which can hardly be achieved with present interferometers. Figs. 4 and 5 show, for example, the visibility and clv of the model Z320 and X300, plus the fitted UD, FDD and Gaussian.

Fig. 6 gives the correlation between the visibility and clv distances of the artificial clv's applied to all *true* limb-darkening curves. The small visibility distance range (0 to 3%) compared to the large clv distance range (0 to 27%) shows the low discriminating potential of the visibility in this small spatial frequency region. From Table 2 we see that for each stellar model and for all filters, with the exception of the broad-band filter at 2.2$\mu$m and 3.8$\mu$m, and a handful model/narrow-band filter combinations, FDD is the best fitting model. For the broad-band filters at 2.2$\mu$m and 3.8$\mu$m, and the X-, Z- and U-series models with $T_{eff}$ = 3200 K, 3350 K and 3500 K, UD is the best fitting model. For the model/narrow-band filter combinations 0.58/X335, 0.59/X335, 0.70/X320, 0.71/X350 and 0.75/X300, FDD and Gaussian are equally good fitting models.

Interferometric stellar visibility measurements which include the central visibility maximum only are not able to distinguish between different theoretical limb-darkening curves, whereas this may be possible with measurements including additionally the first local UD visibility maximum. To show this we have performed additional fits to the *true* limb-darkening curves with the latter mentioned larger spatial frequency range. Fig. 7 shows correlations as in Fig. 6 (top), but for those distance pairs only where the clv distance of the FDD model is smaller than 4%, (i.e. in these cases the *true* limb-darkening is nearly a perfect FDD). From Fig. 7 we see, that one can distinguish between the *true* FDD model and the wrong UD model: a) if the average error of the measured visibility is smaller than about 0.3% for the small spatial frequency fit region (= up to the first null of the corresponding UD visibility), and b) if the visibility error is smaller than only about 1.8% for the larger fit region (= including the first null and the first local maximum of the corresponding UD visibility). The former small visibility error ($\sim 0.3\%$) may hardly be achievable with interferometers, whereas the latter one ($\sim 1.8\%$) can be achieved with interferometers. The limb-darkening measurements of $\alpha$ Bootis with the Mark III interferometer (Quirrenbach et al. 1996) confirm the above required error limit (their measurements had $\sim 1.5\%$ average visibility error up to, approximately, the first local maximum of the corresponding UD visibility).

Hestroffer (1997) has proposed a one-parameter representation of the clv, $I_\lambda(\mu) = \mu^\alpha$, which is impressively flexible and provides very good clv fits within a wide range of different realistic limb-darkening shapes. Hestroffer's representation which includes the UD ($\alpha$ = 0) and the FDD ($\alpha$ = 1) cases may well describe the typical transition from near-UD to near-FDD shapes ($0 < \alpha < 1$) often found as one follows continuum limb-darkening from long towards short wavelengths, and also yields the Gauss-type shapes (large $\alpha$) sometimes occurring in very extended configurations. It avoids the un-physical clv discontinuity at $\mu$ = 0 of all limb-darkening approximations (except their 'fully darkened' limits) derived from compact models, resulting from semi-infinity even in the surface layers of a strictly plane-parallel statification. In this representation, the position of the zero-intensity layer defining the cosine $\mu$ of the angle between the line of sight and the radius vector defines a monochromatic or filter radius. Thus, Hestroffer's parametrization seems to be well suited for more elaborate studies of extended-atmosphere stars, and we may offer to calculate fit values equivalent to those of Table 2 for this representation too, if specific very-high-accuracy observations are to be evaluated.

Sample applications of Hestroffer's parametrization are shown in Figs. 8 and 9 for the 1.04$\mu$m filter in model U250 and the 0.71$\mu$m filter in model X250, respectively. Both clv curves are not well represented by the $\alpha$ = 1 FDD limit (8% fitting accuracy in Table 2) whereas Hestroffer's power law approximation with $\alpha$ = 0.5 (Fig. 8) and $\alpha$ = 2.8 (Fig. 9) provides excellent fits to the model-predicted intensities. In terms of visibilities, however, observation of the side-maximum with an accuracy of the order of a few percent would be needed in order to tell apart a power difference of $\Delta\alpha$ = 1.

## 7. Discussion

It is obvious from our visibility fits and the resulting entries in Table 2 that the FDD curve often is a surprisingly good approx-

imation to the model-predicted limb-darkening shape. Even at long continuum wavelengths in the hottest low-extension models where the intensity decreases rather sharply towards the edge of the disk the FDD is a better approximation than the UD adopted in most published reductions of observational data. Thus, we recommend using a FDD clv whenever data of cool non-Mira M giants are to be reduced and modelled clv shapes are not available. Resulting monochromatic 'FDD-radii' are in most cases only a few percent larger than $\tau = 1$ radii and comparable to radii defined by the 10% intensity level also entered in Table 2, but deviations from this rule do occur. Scaling of published 'UD-radii' to FDD- or $\tau = 1$ radii can be done with due caution by means of the numbers given in the tables. Gauss-type limb-darkening (or large-$\alpha$ cases in Hestroffer's parametrization) is untypical in non-Miras and Gauss fits reach the quality of FDD fits only in a very few cases.

Generally, correct assumptions about limb-darkening become more and more crucial with decreasing effective temperature of the star and increasing geometrical extension of its atmosphere. Comparison, for instance, in Table 2 of monochromatic radii in the 0.71 strong TiO and the neighboring 0.75 inter-band feature in X280 and X250 shows that FDD or UD data reduction feigns significantly smaller radii inside than outside the band although, of course, the opposite is true in terms of $\tau = 1$ radii indicating the region of photon origin and 10% radii hardly differ.

The tables also show that real-continuum wavelengths to be used for safely measuring effective temperatures are only found in the blue and in the infrared region above 1 $\mu$m. Other frequently observed near-continuum 'windows' at shorter wavelengths are contaminated by TiO band absorption at low temperatures, and typical corrections for obtaining real-continuum radii may be estimated from our tables.

*Acknowledgements.* We thank W. Duschl, A. Gauger and G. Weigelt for valuable comments.

## References

Baschek B., Scholz M., Wehrse R. 1991, A&A 246, 374
Bessell M.S., Brett J.M., Scholz M., Wood P.R. 1989a, A&AS 77,1 (BBSW; erratum: 87, 621)
Bessell M.S., Brett J.M., Scholz M., Wood P.R. 1989b, A&A 213, 209
Bessell M.S., Brett J.M., Scholz M., Wood P.R. 1991, A&AS 89, 335 (BBSW)
Bessell M.S., Scholz M., Wood P.R. 1996, A&A 307, 481
Bogdanov M.B., Cherepashchuk A.M. 1990, SvA 34, 393
Claret A., Diaz-Cordoves J., Giminez A. 1995, A&AS 114, 247
Di Benedetto G.P. 1993, A&A 270, 315
Diaz-Cordoves J., Claret A., Giminez A. 1995, A&AS 110, 329
Dyck H.M., Benson J.A., van Belle G.T., Ridgway S.T. 1996, AJ 111, 1705
Haniff C.A., Scholz M., Tuthill P.G. 1995, MNRAS 276, 640
Hestroffer D. 1997, A&A 327, 199
Manduca A. 1979, A&AS 36, 411
Manduca A., Bell R.A., Gustasson B. 1977, A&A 61, 809
Quirrenbach A., Mozurkewich D., Buscher D.F., Hummel C.A., Armstrong J.T. 1996, A&A 312, 160
Ridgway S.T., Joyce R.R., White N.M., Wing R.F. 1980, ApJ 235, 126
Scholz M. 1997, in: Bedding T.R., Booth A.J., Davis J. (eds.) Fundamental Stellar Properties: The Interaction between Observation and Theory, IAU Symp. 189, Kluwer, Dordrecht, p. 51
Scholz M., Takeda Y. 1987, A&A 186, 200 (erratum: 196, 342)
Tuthill P.G., Haniff C.A., Baldwin J.E., Feast M.W. 1994, MNRAS 266, 745
Van Hamme W. 1993, AJ 106, 2096